

ORIGINAL ARTICLE

# Mechanical Programming of Soft Actuators by Varying Fiber Angle

Fionnuala Connolly,<sup>1</sup> Panagiotis Polygerinos,<sup>1,2</sup> Conor J. Walsh,<sup>1,2</sup> and Katia Bertoldi<sup>1,3</sup>

## Abstract

In this work we investigate the influence of fiber angle on the deformation of fiber-reinforced soft fluidic actuators. We demonstrate that, by simply varying the fiber angle, we can tune the actuators to achieve a wide range of motions, including axial extension, radial expansion, and twisting. We investigate the relationship between fiber angle and actuator deformation by performing finite element simulations for actuators with a range of different fiber angles, and we verify the simulation results by experimentally characterizing the actuators. By combining actuator segments in series, we can achieve combinations of motions tailored to specific tasks. We demonstrate this by using the results of simulations of separate actuators to design a segmented wormlike soft robot capable of propelling itself through a tube and performing an orientation-specific peg insertion task at the end of the tube. Understanding the relationship between fiber angle and motion of these soft fluidic actuators enables rapid exploration of the design space, opening the door to the iteration of exciting soft robot concepts such as flexible and compliant endoscopes, pipe inspection devices, and assembly line robots.

## Introduction

IN RECENT YEARS, significant attention has been devoted to the study of soft, fluidic actuators, because of their compliance, easy fabrication, and ability to achieve complex motions with simple control inputs.<sup>1–6</sup> These unique capabilities have led to a variety of innovative potential applications in the areas of medical devices,<sup>7,8</sup> search and rescue devices,<sup>9</sup> and assistive robots.<sup>10</sup> One of the most well-known and widely used pneumatic soft actuators is the McKibben actuator,<sup>11–13</sup> which upon pressurization produces a simple axial contraction and radial expansion motion. This actuator has been studied in detail and has been shown to have many uses.<sup>14–16</sup> However, in order to increase the applicability of soft robots, it is desirable to have access to a library of actuators capable of producing a much wider range of motions. In an effort to increase functionality in soft actuators, multiple McKibben actuators have been combined to produce more complex twisting motions.<sup>7,17</sup> Furthermore, bending motions have been achieved using PneuNets<sup>2–5</sup> and flexible microactuators,<sup>18</sup> and a wider range of motions, including extension, twisting, and bending, has been demonstrated by using fillers (paper or fabric) in elastomer composites,<sup>4</sup> fiber-reinforced elastomers,<sup>18</sup> and combinations of elastomers with

different stiffnesses.<sup>19</sup> However, in order to simplify and accelerate the design of soft robots, there is still a need to develop actuators that can be easily fabricated and designed and easily programmed to produce a wide range of motions, and that can be used as building blocks to realize more complex motions, such as locomotion and burrowing.

We looked to nature for inspiration for the realization of such actuators and noted that fiber-reinforced structures are ubiquitous. For example, nemertean and turbellarian worms have an outer layer of helically arranged collagen fibers to limit the elongation and contraction of the worm's body,<sup>20,21</sup> and the walls of arteries are strengthened with a helical arrangement of collagen fibrils.<sup>22</sup> Moreover, fiber-reinforced structures in nature often function as actuators. Examples include the body of the earthworm,<sup>23</sup> the tube feet of starfish,<sup>24</sup> and soft muscular systems of the human body, such as the heart.<sup>7</sup> Furthermore, we notice that the nonlinear theory of anisotropic tubes<sup>25–28</sup> and, more recently, simple kinematics models<sup>29,30</sup> have shown that pressurized fiber-reinforced hollow cylinders are capable of many motions, including axial extension, radial expansion, and twisting.

In this article, we aim to design a mechanically programmable soft actuator whose response can be tuned via how fibers are oriented in its construction. We explore numerically

<sup>1</sup>School of Engineering and Applied Sciences, <sup>2</sup>Wyss Institute for Biologically Inspired Engineering, and <sup>3</sup>Kavli Institute for Bionano Science and Technology, Harvard University, Cambridge, Massachusetts.

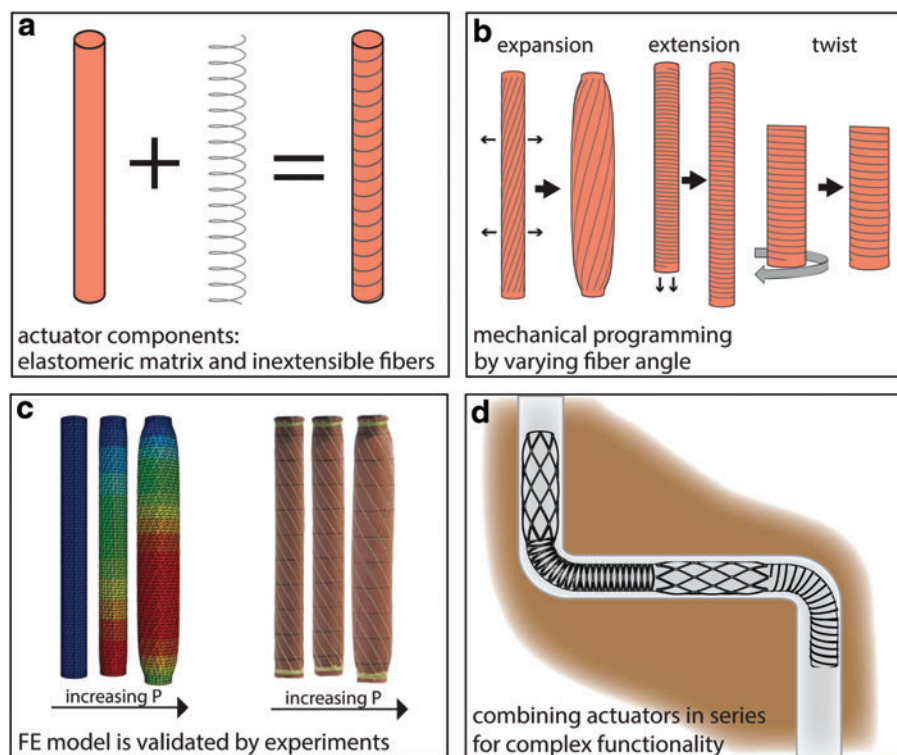


**FIG. 1.** Fiber-reinforced soft actuators. **(a)** The actuators consist of an elastomeric matrix surrounded by a helical arrangement of fibers. **(b)** The actuators can expand, extend, or twist upon pressurization. **(c)** A combination of finite element modeling and experimental characterization is used to explore the motions that can be achieved. **(d)** Combining actuator segments in series, we can achieve combinations of motions tailored to specific tasks. For example, we can combine extending and expanding segments to create a robot capable of navigating through a pipeline. Color images available online at [www.liebertpub.com/soro](http://www.liebertpub.com/soro)

and experimentally the response of fluidic-powered cylindrical elastomeric actuators, with fibers wound in a helical pattern around the outside of the actuator, as shown in Figure 1a and 1c. While previous work has demonstrated that this type of fiber-reinforced actuator is capable of many types of motions,<sup>7,8,11–18</sup> here we study in detail the effect of fiber angle (the angle between the horizontal axis and the fiber) on actuator motion. Our results indicate that, by simply varying the fiber angle, we can design actuators that change in length, change in radius, and twist about their axis, as shown in Figure 1b. We also demonstrate that, by using multiple families of fibers (i.e., fibers arranged at different angles), we can expand the actuator design space and have greater flexibility in the type of actuator we can create. We show that these systems can be efficiently designed using numerical simulations, which enable rapid exploration of the design space. Furthermore, by combining actuator segments in series, as shown in Figure 1d, for example, we can achieve combinations of motions tailored to specific tasks, such as peristaltic locomotion and burrowing.

## Results and Discussion

To characterize the effect of fibers on the response of the actuators, we begin by studying them numerically using finite element analysis. Such an approach facilitates accurate modeling of the system, incorporating material properties and the effect of the fiber reinforcement. It also enables much more rapid exploration of the design space compared with fabricating and experimentally characterizing multiple actuators, and therefore can be effectively used to design actuators tailored to specific tasks. We used the commercial finite element package Abaqus, version 6.12-1 (SIMULIA, Providence, RI), to run simulations for actuators

with a range of different fiber angles, varying from  $0^\circ$  (circumferential fibers) to  $90^\circ$  (axial fibers) (see Supplementary Video S1; see also Supplementary Data for details of how the simulations were performed; Supplementary Data are available online at [www.liebertpub.com/soro](http://www.liebertpub.com/soro)). During the simulations, we monitored (1) the change in the radius of the actuator ( $b/B$ ), (2) the change in length of the actuator ( $\lambda_z = l/L$ ), and (3) the amount by which the actuator twists about its longitudinal axis ( $\tau$ ) (see Supplementary Data for details on how to extract these quantities from the simulations).

We first focus on actuators with a single family of fibers (i.e., all fibers have the same orientation), and in Figure 2a we plot  $\lambda_z$ ,  $b/B$ , and  $\tau$  as a function of the applied pressure for fiber angles varying from  $\alpha = 0^\circ$  to  $\alpha = 90^\circ$ . As expected, for  $\alpha = 0^\circ$ , corresponding to circumferential fibers, the motion of the actuator is constrained only in the radial direction, and so we see in the plot of axial extension versus pressure that maximum axial extension occurs for this angle. As  $\alpha$  is increased from  $0^\circ$ , radial expansion increases and axial extension decreases until finally, at  $\alpha = 90^\circ$  (axial fibers), we have maximum radial expansion and no axial extension. We also see that for fiber angles in the  $50^\circ$ – $90^\circ$  range, the axial stretch is nonmonotonic, as the length of the actuator first decreases and then increases as pressure increases. Finally, by plotting twist per unit length as a function of pressure, we note that at  $0^\circ$  and  $90^\circ$ , the fibers are arranged symmetrically, and so there is no twist about the axis. We also see the unintuitive result that twist peaks around  $30^\circ$ .

To verify the finite element results, we compared numerical predictions and experimental data for two actuators characterized by  $\alpha = -3^\circ$  and  $\alpha = 70^\circ$  (see Supplementary Video S2). From the finite element analysis, we expect that these actuators will exhibit contrasting behavior upon pressurization. Upon completion of the fabrication (see Supplementary Data for

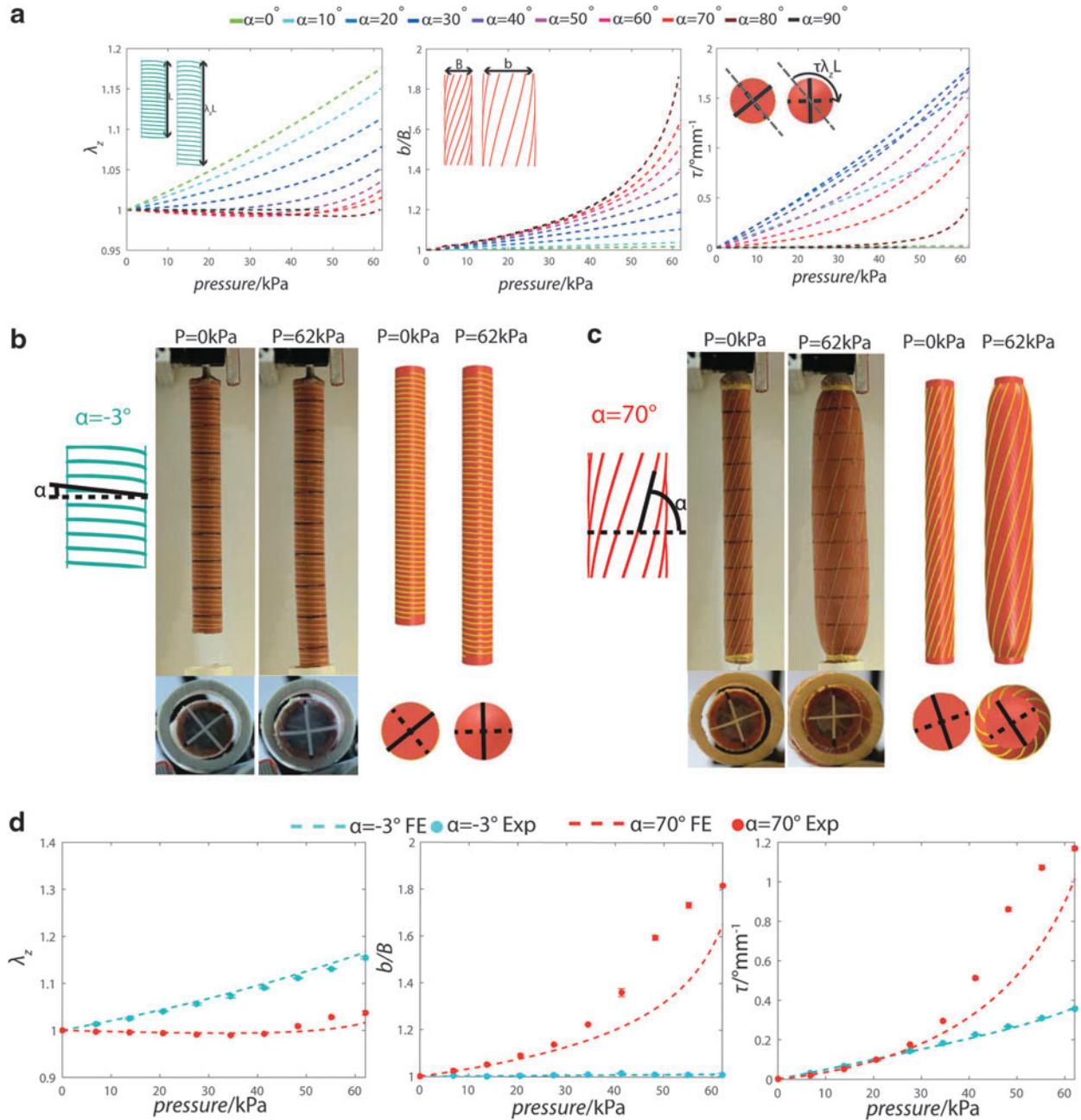


**FIG. 2.** Actuators with one family of fibers. **(a)** Finite element results showing extension ( $\lambda_z$ ), expansion ( $b/B$ ), and twist per unit length ( $\tau$ ) as a function of the applied pressure for a range of different fiber angles. Note that we define the positive fiber orientation to be in the clockwise direction. Positive fiber orientation induces twist in the counter-clockwise direction (negative twist). However, here we are interested in comparing the magnitude of the twist for different angles, and so we plot the magnitude of the twist (rather than magnitude and direction). **(b)** Photographs from experimental characterization (left) and snapshots from finite element simulation (right) for an actuator with fiber angle  $\alpha = -3^\circ$ . Both front views (top) and bottom views (bottom) are shown. **(c)** Photographs from experimental characterization (left) and snapshots from finite element simulation (right) for an actuator with fiber angle  $\alpha = 70^\circ$ . **(d)** Comparison between finite element simulations and experiments for two actuators with fiber angle  $\alpha = -3^\circ$  and  $\alpha = 70^\circ$ . The error bars on the experimental results show the standard deviation from the mean result obtained by pressurizing each actuator three times. As in Figure 2a, the magnitude of the twist is plotted here, rather than magnitude and direction. Color images available online at [www.liebertpub.com/soro](http://www.liebertpub.com/soro)

details), we pressurized each actuator to 62.05 kPa and took pictures of the actuator during the loading process. By tracking markings on the actuator (see Fig. 2b and 2c), we could analyze the change in radius and length. To obtain values for the twist, we placed a camera underneath the actuator and used

markings to track the center and four points on the circumference of the bottom of the actuator.

In the same way as for the finite element simulations, we plotted the axial stretch, circumferential stretch, and twist per unit length, as functions of pressure (see Supplementary Data

for details). The results are reported in Figure 2d. In the case of  $\alpha = -3^\circ$ , we see excellent agreement between experimental and numerical results. For  $\alpha = 70^\circ$ , the match is very good at lower pressures, with some deviation at higher pressures due to the highly nonlinear response exhibited by the actuator. In particular, for  $\alpha = -3^\circ$  we see that the actuator twists about its axis and extends axially, with little change in the radial dimension. In contrast, for  $\alpha = 70^\circ$  the actuator twists, expands radially, and undergoes slight axial contraction in response to pressurization. Finally, we note that the discrepancies between the numerical and experimental results are likely due to imperfections in the experiments, and end effects that lead to nonuniform deformations. Having verified the finite element results, we can use the graphs in Figure 2a to design an actuator that maximizes or minimizes extension, expansion, or twist. Also, by combining the results from the three graphs, we can design actuators with specific characteristics, such as an actuator that maximizes twist while minimizing change in radius, or one that maximizes twist and extension.

Although varying the fiber angle of an actuator yields a range of different motions, there are some motions that are more difficult to achieve than others. For example, a pure extending actuator requires a fiber angle of  $0^\circ$ , but achieving this in practice is difficult due to variations in the fabrication process. To overcome this issue, we can add a second family of fibers to the first one. This second family of fibers can be arranged at any angle, leading to a variety of different motions that can be achieved. However, note that if we arrange the two families of fibers symmetrically, there is no twist; the actuator purely extends or expands. We demonstrate this by characterizing an actuator with fibers arranged at  $\alpha_1 = 3^\circ$  and  $\alpha_2 = -3^\circ$  (see Supplementary Videos S3 and S4). We see in Figure 3a that the behavior in the axial and radial directions is very similar to the case with only one family of fibers (axial extension and slight radial expansion), but now the new family of fibers cancels the twist.

As well as yielding an actuator that does not twist, adding a second family of fibers also expands the design space for this class of actuators. For instance, we can fabricate multiple actuators that have similar twist per unit length as a function of pressure, but different behavior in the axial and radial directions (see Supplementary Videos S5 and S6). We performed a range of finite element simulations and identified a pair of actuators that exhibit this behavior: an actuator with fibers at  $\alpha_1 = 17^\circ$  and  $\alpha_2 = -67^\circ$ , and one with fibers at  $\alpha_1 = 60^\circ$  and  $\alpha_2 = -11^\circ$ . In Figure 3b, we compare the response, both experimental and numerical, of these two actuators. We see that the two actuators have almost the same curve for twist as a function of pressure and neither sees much change in radius. However, one actuator extends upon pressurization, while the other contracts. So we see that adding an extra family of fibers expands the design space, giving us greater flexibility in the type of actuator we can create.

The actuators presented here have potential to be used in a wide variety of applications. For example, we can combine them to fabricate a device capable of propelling itself through a tube with a  $90^\circ$  bend in it and performing an orientation-specific peg insertion task at the end (see Supplementary Video S7). To design such devices, we took inspiration from the peristaltic locomotion of the earthworm.<sup>23</sup> The earthworm uses longitudinal and circumferential muscles to con-

tract the segments of its body sequentially, enabling it to move forward. Therefore, we assembled four actuators in series, as shown in Figure 4a, with segments 1, 2, and 3 responsible for propelling the device through the tube and segment 4 designed to twist the prongs into the holes.

More specifically, actuator segments 1 and 3 were required to expand and anchor the device in the tube, and so we chose to arrange the fibers symmetrically at  $70^\circ$  and  $-70^\circ$  to achieve a balance between maximum expansion and ease of fabrication. To choose the dimensions of the actuators, we took advantage of finite element analysis. Considering a tube with an inner diameter of 13 mm, we performed a range of finite element simulations and found that an actuator with an outer diameter of 8 mm, a wall thickness of 1 mm, and fibers symmetrically arranged at angles of  $70^\circ$  and  $-70^\circ$  would expand to give an outer diameter of 14.5 mm at a pressure of 100 kPa, and this would be sufficient to act as an anchor. In contrast to the anchoring segments, the function of segment 2 was to achieve extension and move the device forward, and so we arranged the fibers symmetrically at  $7^\circ$  and  $-7^\circ$ . The actuation sequence required for forward locomotion is shown in Figure 4b. Each segment of the device is actuated independently. When we actuate segment 1, it expands and anchors the device in the tube. Segment 2 extends to move the device forward. Segment 3 expands to anchor the device in the forward position, and we can then depressurize segments 1 and 2. It is key to note that, since all of the segments are completely soft, the bend in the tube is easily negotiated (see Figure 4b center). This would be much more difficult to achieve if rigid components were used.

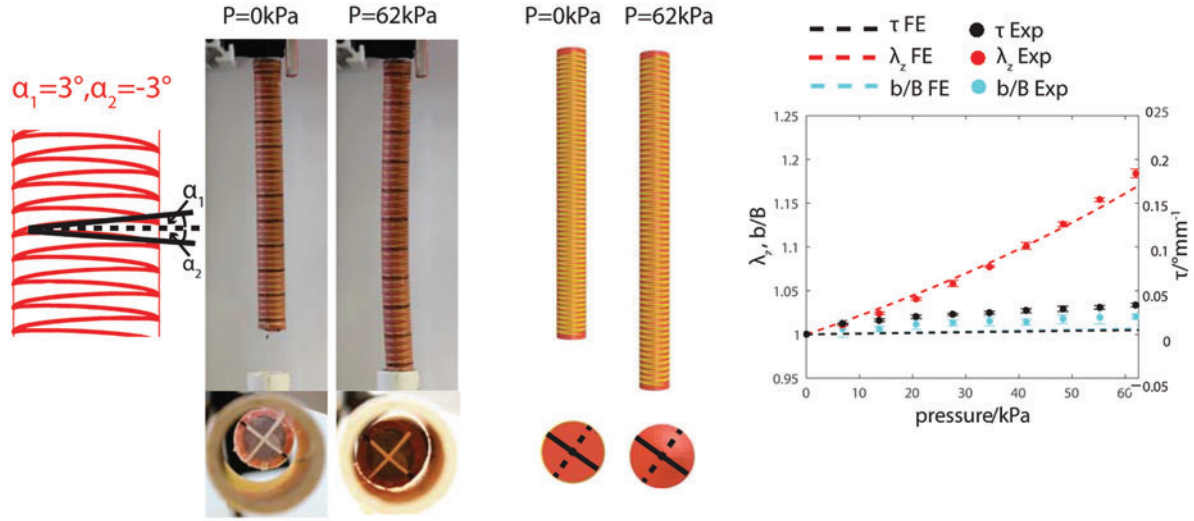
When the device reaches the end of the tube, we then want it to insert the two prongs at its front into two holes. Since the prongs are typically misaligned (see Figure 4c), we actuate segment 4, whose fibers are arranged asymmetrically, at an angle of  $10^\circ$ , to achieve a balance of extension and twisting. As shown in Figure 4c, the prongs easily twist into the holes and we can use segments 1, 2, and 3 to adjust the position of the device if necessary. Since the device has intrinsic passive compliance, even if the front segment is not exactly centered in the tube, the prongs still find their way into the holes.

## Conclusions

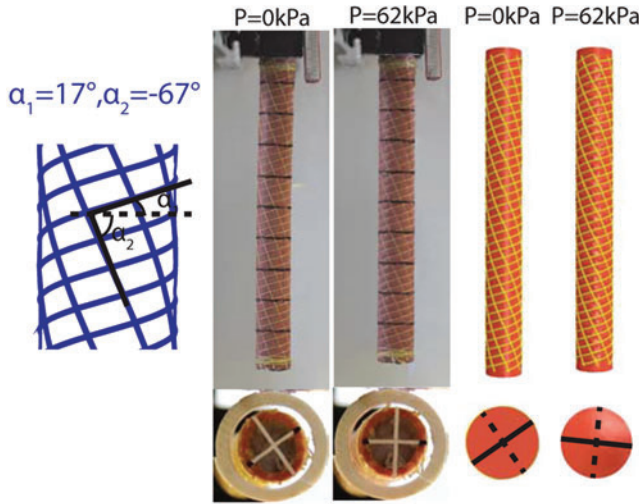
We have shown that, by simply varying the fiber angle of fluidic-powered fiber-reinforced soft actuators, we can tune their response to achieve a wide range of motions. Finite element simulations accurately model the relationship between fiber angle and output motion, and we can use the results of these simulations to guide the design of soft actuators and greatly accelerate the design process. Future challenges in this area will include optimization of the simulations to reduce computation time while still maintaining accuracy, inclusion of dynamic effects in the simulations, refinement of the fabrication procedure, and the development of analytical models for use in real-time controllers. We highlight the utility of knowledge gained from the simulations by mechanically programming multiple soft actuator segments and combining them in series to create a wormlike soft robot that can navigate through a pipe and complete a simple insertion task. The ability to understand how tailoring of the fiber angle influences the motion of the soft actuators enables rapid exploration of the design space for this class of soft actuators and



**a** symmetric fibers



**b** asymmetric fibers



**c** asymmetric fibers

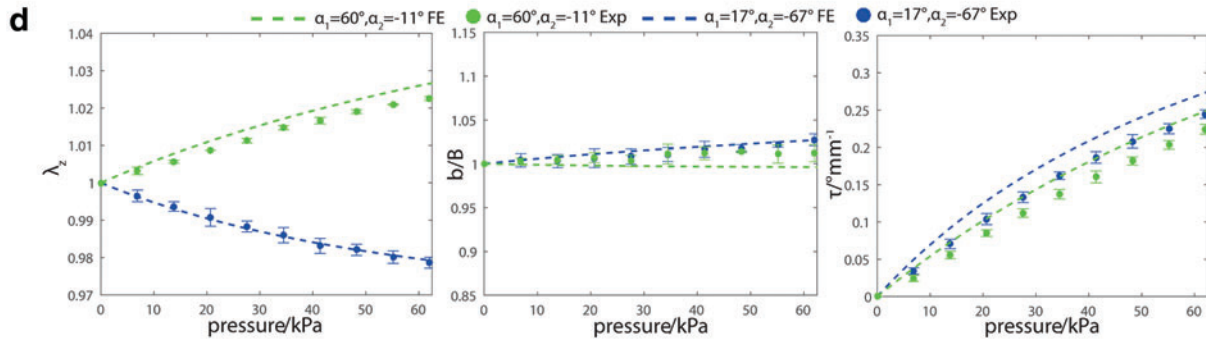
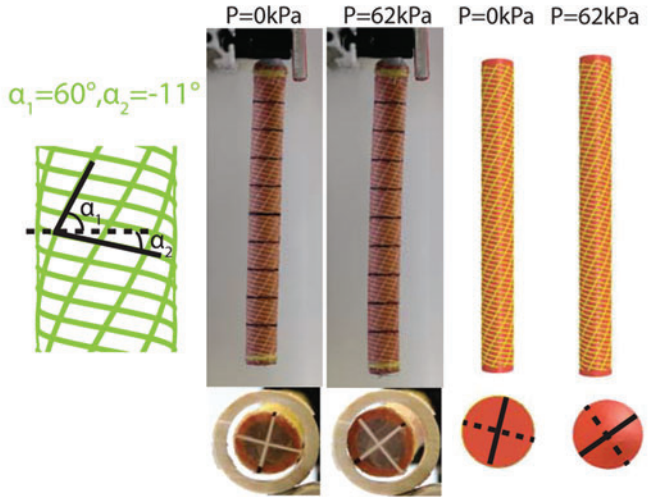


**FIG. 3.** Actuators with two families of fibers. **(a)** Photographs from experimental characterization (*left*), snapshots from finite element simulation (*center*), and comparison between finite element and experimental results (*right*) for an actuator with fibers symmetrically arranged at  $\alpha_1 = 3^\circ$  and  $\alpha_2 = -3^\circ$ . The error bars show the standard deviation from the mean result obtained by pressurizing each actuator three times. **(b)** Photographs from experimental characterization (*left*) and snapshots from finite element simulation (*right*) for an actuator with fibers at  $\alpha_1 = 17^\circ$  and  $\alpha_2 = -67^\circ$ . **(c)** Photographs from experimental characterization (*left*) and snapshots from finite element simulation (*right*) for an actuator with fibers at  $\alpha_1 = 60^\circ$  and  $\alpha_2 = -11^\circ$ . **(d)** Comparison between finite element and experimental results for an actuator with fibers at  $\alpha_1 = 17^\circ$  and  $\alpha_2 = -67^\circ$  and an actuator with fibers at  $\alpha_1 = 60^\circ$  and  $\alpha_2 = -11^\circ$ . The error bars show the standard deviation from the mean result obtained by pressurizing each actuator three times. Color images available online at [www.liebertpub.com/soro](http://www.liebertpub.com/soro)

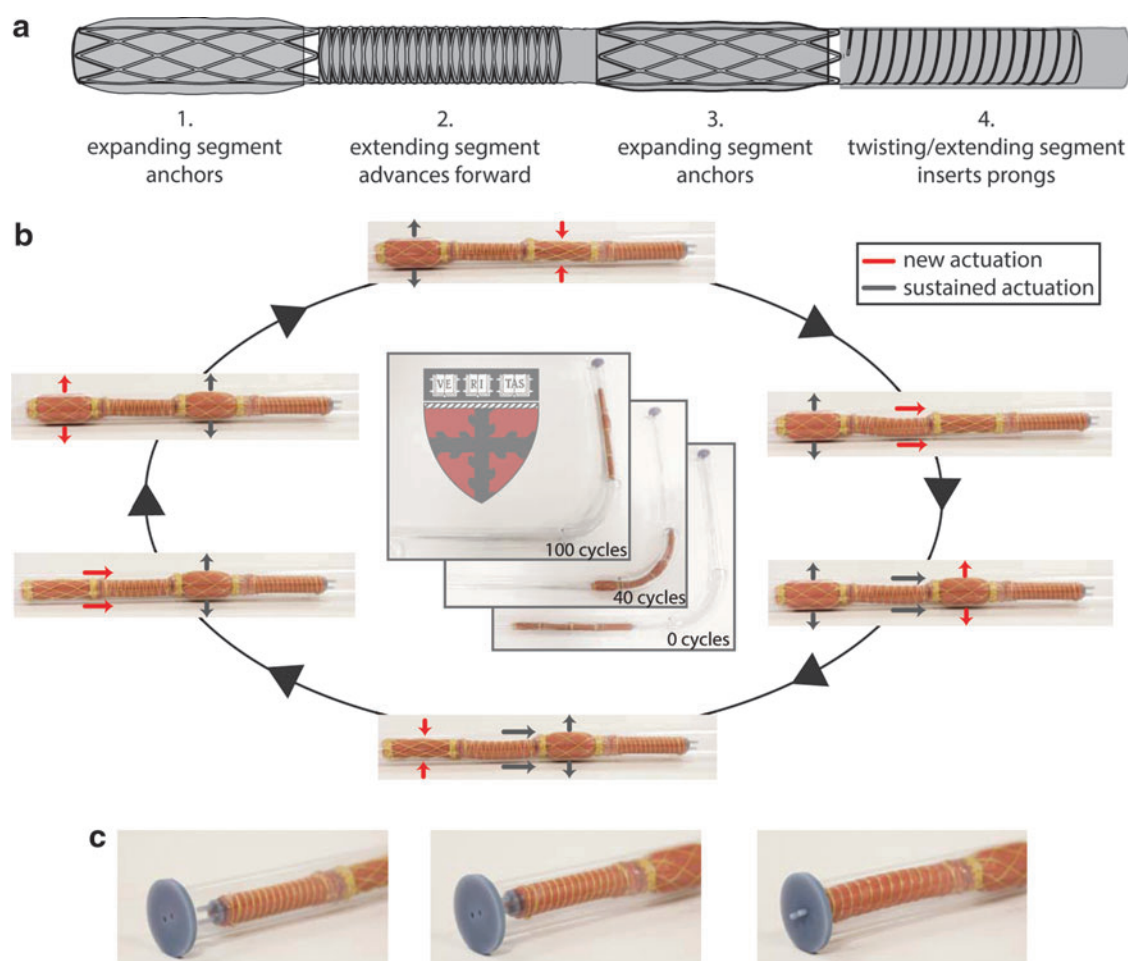


**FIG. 4.** Device capable of propelling itself through a tube and performing an orientation-specific task. **(a)** Four actuator segments are combined in series to achieve forward locomotion and perform an orientation-specific task. **(b)** Segments 1, 2, and 3 are actuated in sequence to move the device through a bent tube. **(c)** As the device approaches the end of the tube, the prongs are not aligned with the holes. Segment 4 is then actuated, extending and twisting the prongs into the holes. Color images available online at [www.liebertpub.com/soro](http://www.liebertpub.com/soro)

the iteration of exciting soft robot concepts such as flexible and compliant endoscopes, pipe inspection devices, and assembly line robots, to name but a few.

### Acknowledgments

This work has been supported by Harvard MRSEC through Grant No. NSF DMR-1420570. K.B. acknowledges support from NSF through Grant No. CMMI-1149456 (CAREER) and by the Wyss Institute through the Seed Grant Program. The authors are grateful to Dr. Kevin Galloway, Johannes Overvelde, Sicong Shan, and Dr. James Weaver for assistance with actuator fabrication, finite element simulations, Matlab tracking code, and 3D printing, respectively.

### Author Disclosure Statement

No competing financial interests exist.

### References

- Wakimoto S, Suzumori K, Ogura K. Miniature pneumatic curling rubber actuator generating bidirectional motion with one air-supply tube. *Adv Robot* 2011;25:1311–1330.
- Ilievski F, Mazzeo AD, Shepherd RF, Chen X, Whitesides GM. Soft robotics for chemists. *Angew Chem Int Ed* 2011; 50:1890–1895.
- Martinez RV, Branch JL, Fish CR, Jin L, Shepherd RF, Nunes RMD, Suo Z, Whitesides GM. Robotic tentacles with three-dimensional mobility based on flexible elastomers. *Adv Mater* 2013;25:205–212.
- Martinez RV, Fish CR, Chen X, Whitesides GM. Elastomeric origami: programmable paper-elastomer composites as pneumatic actuators. *Adv Funct Mater* 2012;22:1376–1384.
- Shepherd RF, Stokes AA, Nunes RMD, Whitesides GM. Soft machines that are resistant to puncture and that self seal. *Adv Mater* 2013;25:6709–6713.
- Majidi C. Soft robotics: a perspective—current trends and prospects for the future. *Soft Robotics* 2013;1:5–11.
- Roche ET, Wohlfarth R, Overvelde JTB, Vasilyev NV, Pigula FA, Mooney DJ, Bertoldi K, Walsh CJ. A bioinspired soft actuated material. *Adv Mater* 2014;26:1200–1206.
- Polygerinos P, Wang Z, Galloway KC, Wood RJ, Walsh CJ. Soft robotic glove for combined assistance and at-home rehabilitation. *Rob Auton Syst* 2014 [E-pub ahead of print]; DOI: 10.1016/j.robot.2014.08.014.
- Tolley MT, Shepherd RF, Mosadegh B, Galloway KC, Wehner M, Karpelson M, Wood RJ, Whitesides GM.

- A resilient, untethered soft robot. *Soft Robotics* 2014;1: 213–223.
10. Sanan S, Ornstein MH, Atkeson CG. Physical human interaction for an inflatable manipulator. *Conf Proc IEEE Eng Med Biol Soc* 2011;2011:7401–7404.
  11. Schulte HF. The characteristics of the McKibben artificial muscle. The application of external power in prosthetics and orthotics. *Natl Acad Sci* 1961;94–115.
  12. Andrikopoulos G, Nikolakopoulos G, Manesis S. A survey on applications of pneumatic artificial muscles. 19th Mediterranean Conference on Control and Automation, MED 2011. IEEE: Piscataway, NJ, 2011, pp. 1439–1446.
  13. Chou CP, Hannaford B. Measurement and modeling of McKibben pneumatic artificial muscles. *IEEE Trans Rob Autom* 1996;12:90–102.
  14. Davis S, Caldwell DG. Braid effects on contractile range and friction modeling in pneumatic muscle actuators. *Int J Robot Res* 2006;25:359–369.
  15. Zhang Z, Philen M. Modeling, analysis and experiments of inter yarn compaction effects in braided composite actuators. *J Compos Mater* 2013;47:3211–3225.
  16. Mortier K. Braided pneumatic muscles for rehabilitation apparatus. Masters dissertation, Politecnico di Torino, 2014.
  17. Pritts MB, Rahn CD. Design of an artificial muscle continuum robot. *IEEE Trans Rob Autom* 2004;5:4742–4746.
  18. Suzumori K, Iikura S, Tanaka H. Flexible microactuator for miniature robots. In: *Proceedings of Micro Electro Mechanical Systems*, Nara, Jan 30–Feb 2, 1991, pp. 204–209.
  19. Konishi S, Nokata M, Jeong OC, Kusada S, Sakakibara T, Kuwayama M, Tsutsumi H. Pneumatic micro hand and miniaturized parallel link robot for micro manipulation robot system. In: *Proceedings of 2006 IEEE International Conference on Robotics and Automation*, Orlando, FL, May 15–19, 2006, pp. 1036–1041.
  20. Cowey JB. The structure and function of the basement membrane muscle system in amphiporus lactifloreus (nemertea). *Q J Microsc Sci* 1952;93:1–15.
  21. Clark RB, Cowey JB. Factors controlling the change of shape of certain nemertean and turbellarian worms. *J Exp Biol* 1958;35:731–748.
  22. Holzapfel GA, Gasser TC, Ogden RW. A new constitutive framework for arterial wall mechanics. *J Elast* 2000;61:1–48.
  23. Quillin KJ. Kinematic scaling of locomotion by hydrostatic animals: ontogeny of peristaltic crawling by the earthworm *lumbricus terrestris*. *J Exp Biol* 1999;202:661–674.
  24. McCurley RS, Kier WM. The functional morphology of starfish tube feet: The role of a crossed-fiber helical array in movement. *Biol Bull* 1995;188:197–209.
  25. Adkins JE, Rivlin RS. Large elastic deformations of isotropic materials X. Reinforcement by inextensible cords. *Philos Trans R Soc A* 1955;248:201–223.
  26. Wang ASD, Ertepinar A. Stability and vibrations of elastic thick-walled cylindrical and spherical shells subjected to pressure. *Int J Nonlinear Mech* 1972;7:539–555.
  27. Haughton DM, Ogden RW. Bifurcation of inflated circular cylinders of elastic material under axial loading-II. Exact theory for thick-walled tubes. *J Mech Phys Solids* 1979;27: 489–512.
  28. Goriely A, Tabor M. Rotation, inversion and perversion in anisotropic elastic cylindrical tubes and membranes. *Proc R Soc London A* 2013;469:20130011–20130011.
  29. Krishnan G, Bishop-Moser J, Kim C, Kota S. Evaluating mobility behavior of fluid filled fiber-reinforced elastomeric enclosures. *Proc ASME Des Eng Tech Conf* 2012;4: 1089–1099.
  30. Bishop-Moser J, Krishnan G, Kim C, Kota S. Kinematic synthesis of fiber-reinforced soft actuators in parallel combinations. *Proc ASME Des Eng Tech Conf* 2012;4:1079–1087.

Address correspondence to:

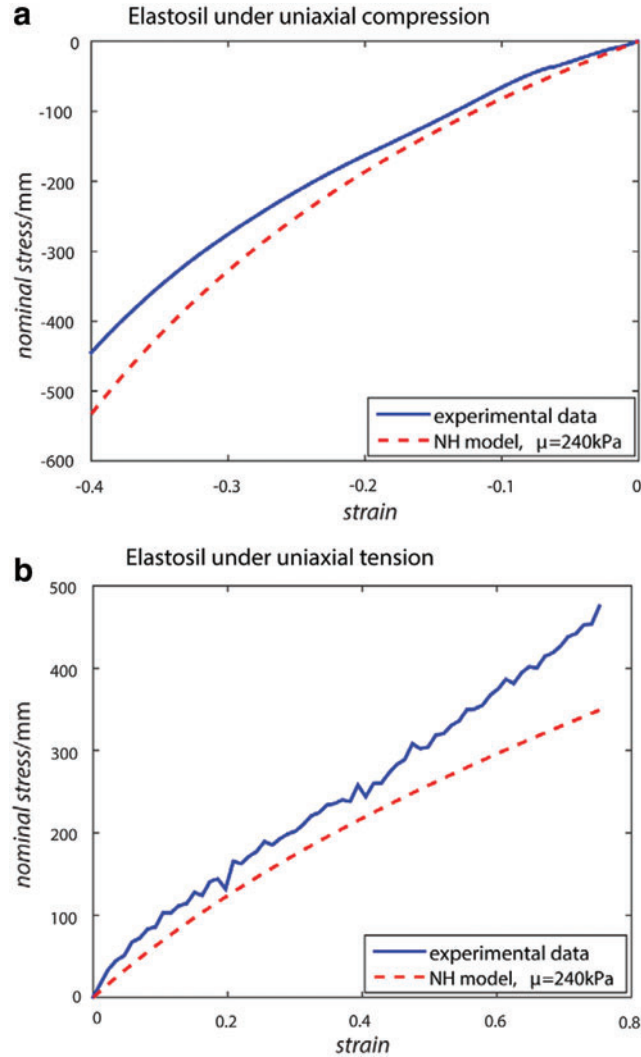
*Conor J. Walsh*  
*School of Engineering and Applied Sciences*  
*Harvard University*  
*Pierce Hall, 29 Oxford Street*  
*Cambridge, MA 02138*  
*E-mail: walsh@seas.harvard.edu*

*Katia Bertoldi*  
*School of Engineering and Applied Sciences*  
*Harvard University*  
*Pierce Hall, 29 Oxford Street*  
*Cambridge, MA 02138*  
*E-mail: bertoldi@seas.harvard.edu*

## Supplementary Data

### Finite Element Modeling

All finite element simulations were performed using the commercial finite element software Abaqus (SIMULIA). The elastomer was modeled as an incompressible neo-Hookean material. A shear modulus of 240 kPa was found by fitting a neo-Hookean model to a stress–strain curve for a cylindrical specimen of Elastosil M4601 (Wacker Chemie AG) under uniaxial compression, and a dogbone-shaped specimen (ASTM standard) under uniaxial tension, as shown in Supplementary Figure S1. The Kevlar fibers were modeled as a linearly elastic material using the manufacturer's specifications: diameter 0.1778 mm, Young's modulus  $31.067 \times 10^6$  kPa, and Poisson's ratio 0.36. Each actuator had inner radius 6.35 mm, wall thickness 2 mm, and length 165 mm. The



**SUPPLEMENTARY FIG. S1.** Stress–strain curve for Elastosil under (a) uniaxial compression and (b) uniaxial tension. The blue line corresponds to the experimental data and the red line to the fit using the neo-Hookean model with an initial shear modulus,  $\mu = 240$  kPa.

density of fiber distribution was approximately 0.36 mm of fiber per  $\text{mm}^2$  of elastomer. For the elastomer, 20-node quadratic brick elements, with reduced integration (Abaqus element type C3D20R), were used, and 3-node quadratic beam elements (Abaqus element type B32) were used for the fibers. The accuracy of the mesh was ascertained through a mesh refinement study and perfect bonding between the fibers and the elastomer was assumed (the fibers were connected to the elastomer by tie constraints). Each simulation required 16,000 elements and 30,000 nodes. Quasi-static nonlinear simulations were performed using Abaqus/Standard. One end of the actuator was held fixed, and a pressure load of 62 kPa was applied to the inner surface of the actuator.

For two cases ( $\alpha = 80^\circ$  and  $\alpha = 90^\circ$ ), the quasi-static simulations were unstable at higher pressures. Therefore, dynamic simulations were performed for these actuators using Abaqus/Explicit and quasi-static conditions were ensured by monitoring the kinetic energy and introducing a small damping factor. The chamber of the actuator was modeled as a fluid-filled cavity, and thermal expansion was used to increase the volume of air inside the cavity. The resulting pressure in the cavity was output, as were the coordinates of the nodes on the outer surface of the actuator, as before.

### Calculating radial stretch, axial stretch, and twist

To calculate the average radial stretch, axial stretch, and twist per unit length of the actuator as a function of the applied pressure, the coordinates of each node on the outer surface of the actuator were output and we focused on the nodes located on two diametrically opposite longitudinal lines, as shown in Supplementary Figure S2a. If we denote with  $L_i$  and  $R_i$  a pair of nodes located on these two lines and characterized by the same initial longitudinal coordinate (i.e.,  $Z_0^{R_i} = Z_0^{L_i}$ ), then the stretch in the radial direction can be calculated as

$$\left(\frac{b}{B}\right)_i = \frac{\sqrt{(X^{R_i} - X^{L_i})^2 + (Y^{R_i} - Y^{L_i})^2}}{\sqrt{(X_0^{R_i} - X_0^{L_i})^2 + (Y_0^{R_i} - Y_0^{L_i})^2}} \quad (\text{S1})$$

where  $(X_0^A, Y_0^A, Z_0^A)$  and  $(X^A, Y^A, Z^A)$  denote the coordinates of node A in the undeformed and deformed configuration, respectively. Moreover, the axial stretch for each pair of nodes can be calculated as

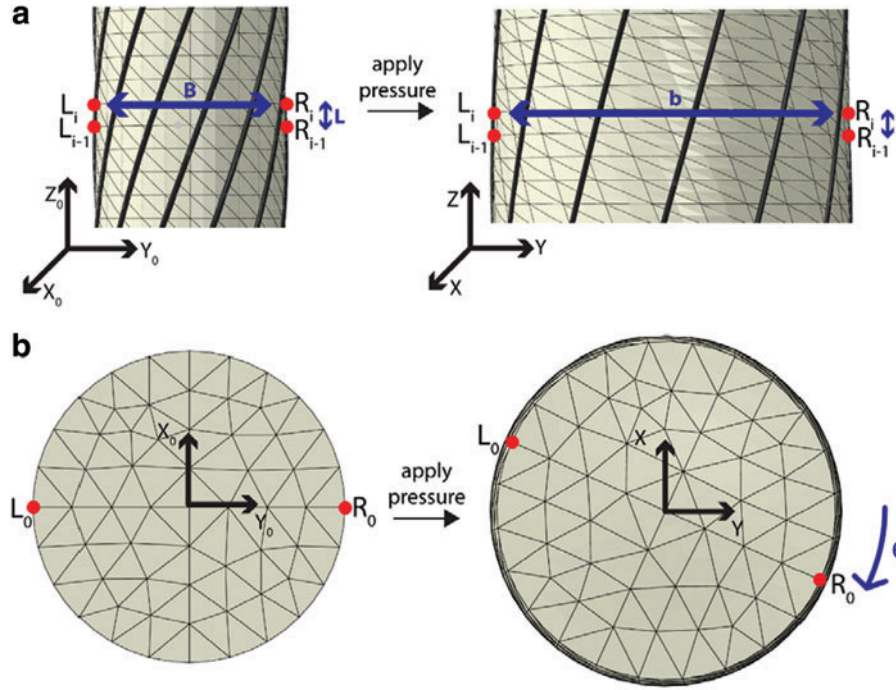
$$\lambda_{z_i} = \frac{Z^{R_i} - Z^{L_i}}{Z_0^{R_i} - Z_0^{L_i}} \quad (\text{S2})$$

Finally, as shown in Supplementary Figure S2b, the twist can be calculated as

$$\theta = \tan^{-1} \left( \frac{X^{R_0} - X_0^{R_0}}{Y^{R_0} - Y_0^{R_0}} \right) \quad (\text{S3})$$

Note that in calculating the average values for the actuator of the radial and axial stretch, only the middle two-thirds of





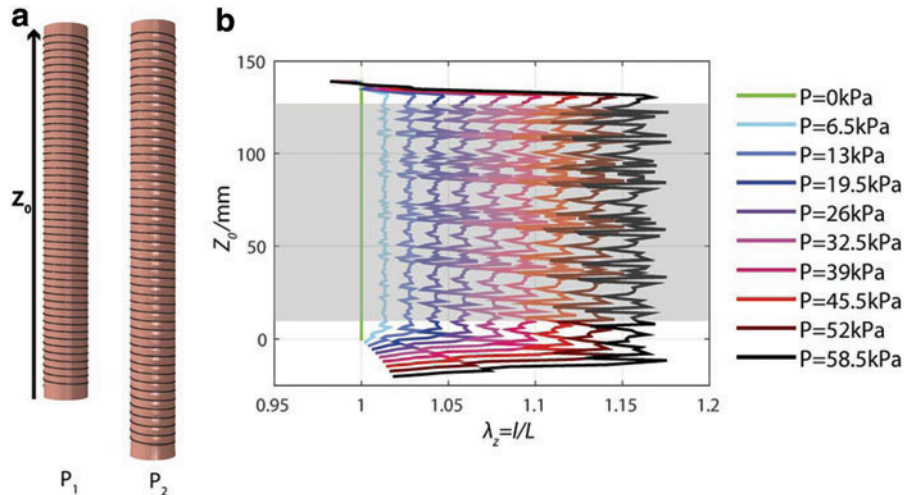
**SUPPLEMENTARY FIG. S2.** Extracting extension, expansion, and twist from the finite element (FE) simulations. **(a)** Pairs of diametrically opposite nodes are used to calculate the radial stretch. Pairs of nodes along the length of the actuator are used to calculate the axial stretch. **(b)** The coordinates of a node on the bottom face of the actuator are tracked to calculate the twist.

the actuator were considered, in order to minimize boundary effects (see Supplementary Figs S3 and S4).

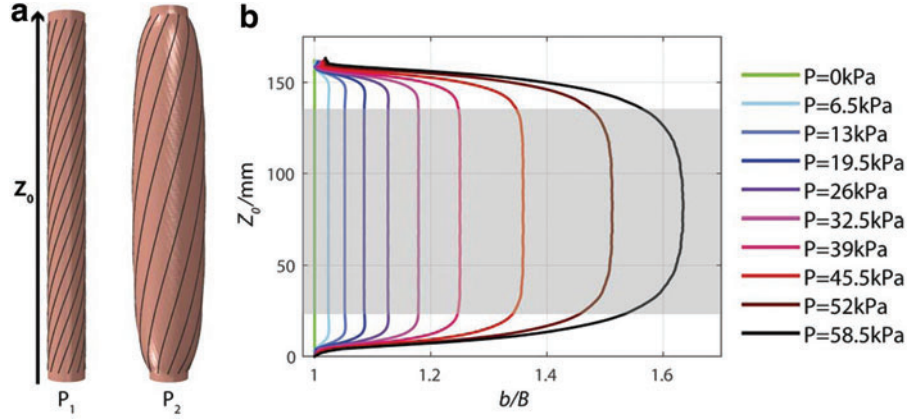
### Fabrication

The actuator mold was designed in Solidworks and 3D printed using an Objet Connex 500 printer (Stratasys) (see Supplementary Fig. S5a). The mold was assembled and held

together firmly with clamps. Elastosil M4601 (Wacker Chemie AG) was poured into the mold (Supplementary Fig. S5b), and degassed in a vacuum chamber for a couple of minutes. A cylindrical metal rod was inserted into the mold to create the core of the actuator. The rod slotted into a round indentation at the bottom of the mold and a 3D printed cap held the rod in place at the top of the mold (Supplementary Fig. S5c). The Elastosil was left overnight at room temperature to



**SUPPLEMENTARY FIG. S3.** FE simulations. Measuring change in length ( $\lambda_z$ ). **(a)** Snapshots of the actuator at  $P_1=0\text{kPa}$  and  $P_2=62\text{kPa}$ . **(b)** Axial stretch of the actuator at each pressure increment, plotted as a function of the longitudinal coordinate  $Z_0$ . Only the results shaded in gray were used to calculate the average values of the length, in order to minimize boundary effects.



**SUPPLEMENTARY FIG. S4.** FE simulations. Measuring change in radius ( $b/B$ ) (a) Snapshots of the actuator at  $P_1=0\text{ kPa}$  and  $P_2=62\text{ kPa}$ . (b) Radial stretch of the actuator at each pressure increment, plotted as a function of the longitudinal coordinate  $Z_0$ . Only the results shaded in gray were used to calculate the average values of the radius, in order to minimize boundary effects.

cure. The next day, the plastic mold was removed. Kevlar fiber was wound in a helical pattern around the outside of the actuator (Supplementary Fig. S5d). Ridges on the surface of the mold left grooves on the actuator, which defined the path for winding the fibers. In this way, we had precise control over the fiber angle.

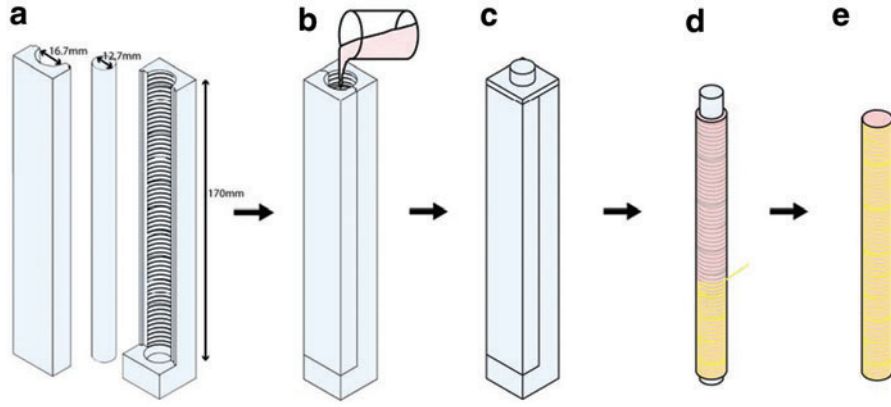
At each end of the actuator, the fiber was looped around a few times and tied. These knots were held in place by applying a small amount of Sil-Poxy (Smooth-On, Inc.). The actuator was then removed from the rod using IPA as a lubricant. The ends of the actuator were plugged with Sil-Poxy, and a vented screw was inserted at one end. The Sil-Poxy was allowed to cure for 24 h. Each actuator had an inner radius of 6.35 mm and a wall thickness of 2 mm. The same materials and a similar procedure were used to fabricate the smaller actuators shown in Figure 4. We used a 3D printed mold of diameter 8 mm and a rod of diameter 6 mm. Sil-Poxy was used to plug the ends of each actuator, and silicone rubber tubing was inserted at one end to provide the air supply. The actuators were glued together with Sil-Poxy.

### Experimental Characterization

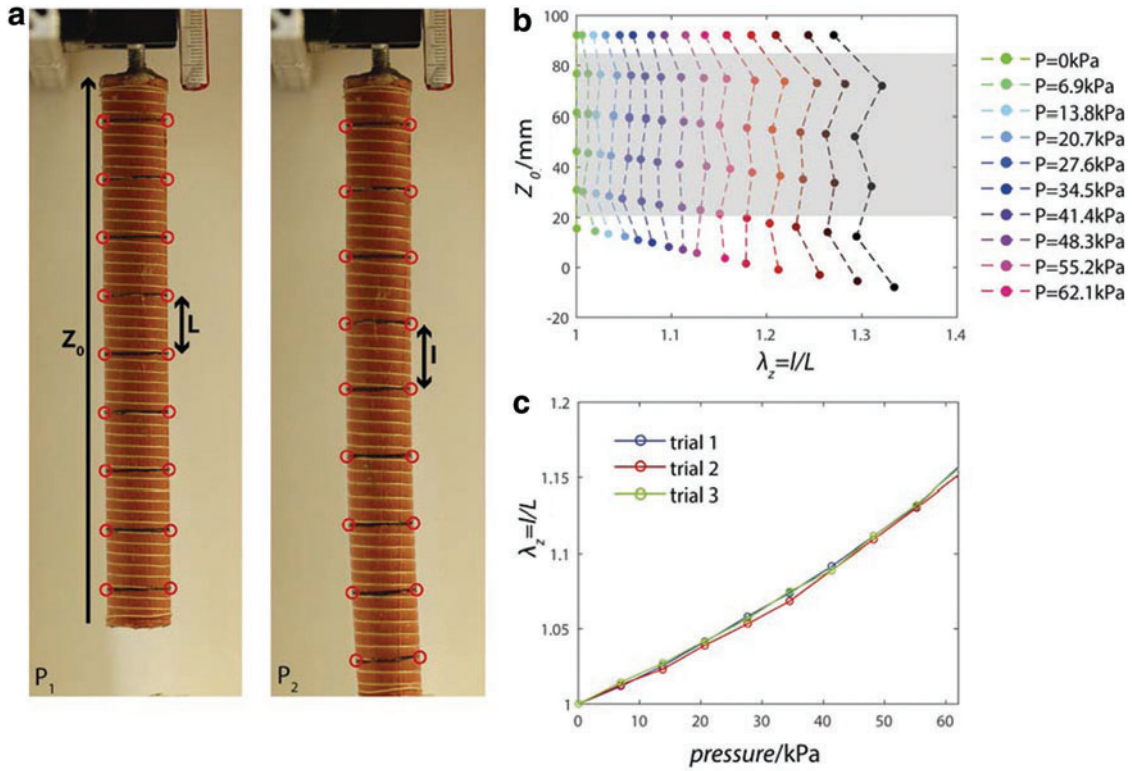
To characterize the deformation of the actuators, each actuator was pressurized to 62.05 kPa, in increments of 6.89 kPa, and the deformation was measured at each incre-

ment. Each actuator was pressurized and depressurized three times, and the results were averaged. To measure the extension and expansion of the actuator, a photograph was taken at each pressure increment with a Canon EOS Rebel T2i camera. Sample photographs are shown in Supplementary Figures S6a and S7a. Black lines were marked on the actuator, and the coordinates of the edges of these lines were tracked using Matlab. The coordinates of the markers were used to calculate the radius and length at points along the actuator (using Eqs. S1 and S2) as shown in Supplementary Figures S6b and S7b. The results were averaged to get the mean expansion and extension, as shown in Supplementary Figures S6c and S7c. Results for the lines near the ends of the actuator were not included, in order to minimize boundary effects.

To measure the twist, the camera was placed underneath the actuator. Lines were marked on the bottom of the actuator, and again, the actuator was pressurized in increments of 6.89 kPa, and a photograph was taken at each increment, as shown in Supplementary Figure S8a. The twist was calculated by using a Matlab script to track the position of four points on the circumference of the actuator. The twist was calculated for each of these points and the results were averaged. The results are shown in Supplementary Figure S8b and S8c. The twist was normalized by calculating twist per unit length, defined as  $\tau = \frac{\theta}{L}$ .

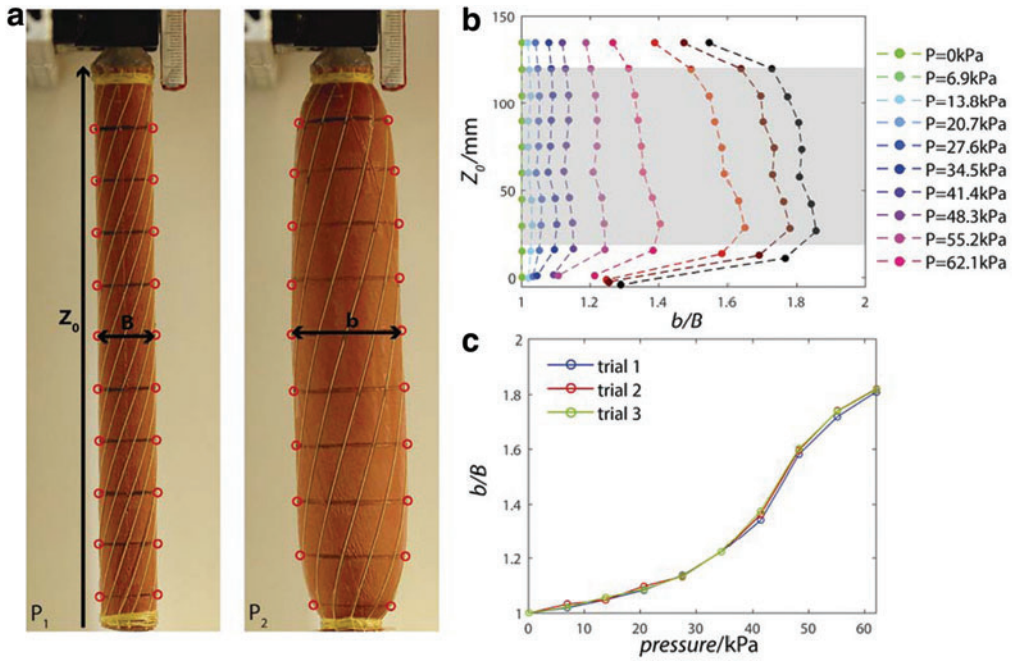


**SUPPLEMENTARY FIG. S5.** Actuator fabrication. (a) A metal rod and 3D-printed mold are used to mold the Elastosil. (b) Elastosil is poured into the mold. (c) The rod is inserted into the mold and held in place with a 3D-printed cap. (d) The mold is removed and Kevlar fiber is wound around the outside of the actuator. (e) The actuator is capped with Sil-Poxy.

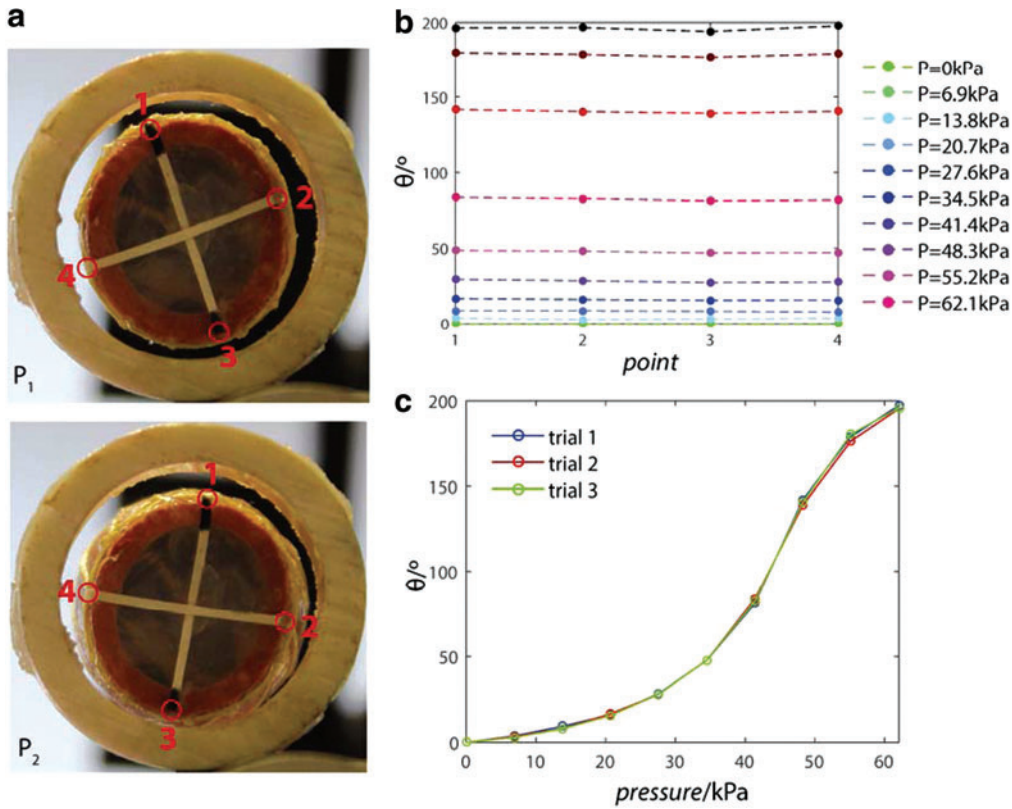


**SUPPLEMENTARY FIG. S6.** Experiments: Measuring the change in length ( $\lambda_z$ ) of an actuator with fiber angle  $\alpha = -3^\circ$ . (a) Photographs of the actuator at  $P_1=0\text{ kPa}$  and  $P_2=62.05\text{ kPa}$ . An alignment feature (which did not interfere with the motion under investigation) was used at the bottom of the actuator. (b) Axial stretch of the actuator at each pressure increment, plotted as a function of the longitudinal coordinate. Only the results shaded in gray were used to calculate the average values of the length, in order to minimize boundary effects. (c) Average value of the axial stretch, plotted as a function of pressure.





**SUPPLEMENTARY FIG. S7.** Experiments: Measuring the change in radius ( $b/B$ ) of an actuator with fiber angle  $\alpha = 70^\circ$ . (a) Photographs of the actuator at  $P_1 = 0$  kPa and  $P_2 = 62.05$  kPa. An alignment feature (which did not interfere with the motion under investigation) was used at the bottom of the actuator. (b) Radial stretch of the actuator at each pressure increment, plotted as a function of the longitudinal coordinate. Only the results shaded in gray were used to calculate the average values of the radius, in order to minimize boundary effects. (c) Average value of the radial stretch, plotted as a function of pressure.



**SUPPLEMENTARY FIG. S8.** Experiments: Measuring the twist ( $\theta$ ) of an actuator with fiber angle  $\alpha = 70^\circ$ . (a) Photographs of the actuator at  $P_1 = 0$  kPa and  $P_2 = 27.58$  kPa. (b) Magnitude of the twist at each point on the circumference of the actuator at different levels of applied pressure. (c) Average value of the twist magnitude, plotted as a function of pressure.